Coalescence Sampling and Analysis of Aerosols using Aerosol Optical Tweezers

Allen E. Haddrell,[1] Rachael E.H. Miles,[1] Bryan R. Bzdek,[1]

Jonathan P. Reid,[1,*] Rebecca J. Hopkins[2,*] and Jim S. Walker[3]

[1] *School of Chemistry, University of Bristol, Bristol, BS8 1TS, UK*

[2] *DSTL, Porton Down, Salisbury, SP4 0JQ, UK*

[3] *BIRAL, Unit 8, Harbour Road Trading Estate, Portishead, Bristol, BS20 7BL, UK*

ABSTRACT

We present a first exploratory study to assess the use of aerosol optical tweezers as an instrument for sampling and detecting accumulation and coarse mode aerosol. A sub-picolitre aqueous aerosol droplet is captured in the optical trap and used as a sampling volume, accreting mass from a free flowing aerosol generated by a medical nebuliser or atomiser. Real-time measurements of the initial stability in size, refractive index and composition of the sampling droplet inferred from Raman spectroscopy confirm that these quantities can be measured with high accuracy and low noise. Typical standard deviations in size and refractive index of the sampling droplet over a period of 200 s are <±2 nm and <±0.0005, respectively, equivalent to <±0.04 % in both measured quantities. A standard deviation of <±1 % over a 200 s period is achieved in the spontaneous Raman intensity measurement. When sampling coarse mode aerosol, mass changes of <10 pg can be detected by the sampling droplet as discrete coalescence events. With accumulation mode aerosol, we show that fluxes as low as 0.068 pg s^{-1} can be detected over a 50 s period, equivalent to ~3 pg of sampled material.

* Corresponding authors: Jonathan P. Reid, j.p.reid@bristol.ac.uk, Tel: +44 117 331 7388; Rebecca H. Hopkins, RJHopkins@mail.dstl.gov.uk, Tel: +44 1980 953 099.

Introduction

Many new techniques for ambient aerosol sampling with off- and on-line analyses have been developed in recent years to determine the chemical composition, mixing state, phase and optical properties of aerosols.[1–3] These include a wide range of mass spectrometric techniques,[4–6] aerodynamic and electrical mobility measurements,[1,3,7] optical techniques such as cavity ringdown spectroscopy and photoacoustic spectroscopy,[8–11] and gas and liquid-chromatographic techniques coupled with mass spectrometry.[12–15] These approaches largely provide access to individual properties. For example, aerosol mass spectrometry allows measurements of size-resolved composition, cavity ringdown spectroscopy leads to the determination of the refractive index of aerosol components, and hygroscopic tandem differential mobility analysis allows an estimation of the hygroscopic response of the aerosol. Correlations in aerosol properties are then inferred from comparing independent measurements made by the different techniques. Here, we report a first step towards a universal sampling and analysis approach for the determination of key aerosol properties using an optically tweezed picolitre solution droplet as a miniature sampling volume.[16,17] Following from our previous work, high accuracy measurements in real-time of the particle size and refractive index (including dispersion),[18–20] composition,[21,22] morphology and phase[23–25] of the sampling droplet could provide a straightforward route to inferring a wide range of fundamental physicochemical properties. These include the refractive indices of ambient aerosol components (water soluble and insoluble, both real and imaginary components of the refractive index),[20] hygroscopic response and phase behaviour,[26,27] the equilibrium gas-particle partitioning of components (vapour pressures),[28,29] and surface activities and viscosities of sampled components (through measurements of droplet surface tension and viscosity derived from particle coalescence timescales).[30–32]

Aerosol optical tweezers (AOT) hold a single aerosol particle in a gradient-force optical trap formed at the focal point of a tightly focussed laser beam.[16,33] The trapping beam not only confines the particle, but acts as an excitation source for probing chemical species within the droplet, leading to the generation of spontaneous Raman scattering by any Raman active molecules. The generated Raman light is backscattered by the trapped droplet and can be collected and imaged by a spectrograph, allowing chemical species within the particle to be identified. Further, the droplet acts as a low loss optical cavity at certain discrete wavelengths within the spontaneous Raman scattering bands leading to an amplification in the Raman intensity at the resonant wavelengths.[34,35] This results in the appearance of sharp stimulated peaks at wavelengths commensurate with

whispering gallery modes (WGMs) on the broad spontaneous Raman band. By comparing the wavelengths at which these resonances occur with calculations of WGM wavelengths from Mie theory, the particle diameter and real part of the refractive index (n-RI) can be determined independently and in real-time.[18,19,35]

The partitioning of a chemical species from the gas phase to the trapped droplet or the accretion of small accumulation mode particles by coalescence leads to a change in the particle radius, n-RI and spontaneous Raman signature.[36,37] The sensitivity with which the AOT technique can detect these changes depends on the magnitude of the change in particle radius, particle refractive index and spontaneous Raman signal, and the accuracy with which these properties can be determined. We have suggested previously that accuracies of $<\pm 2$ nm and $<\pm 0.001$ in radius and n-RI, respectively, are achievable.[18,19,35] By comparing the intensities of two spontaneous Raman bands, the relative proportions of the two chemical species within the droplet can be determined.[22,34,38] Indeed, a detection limit of 4 pg of sodium nitrate (with a Raman cross-section of 7.9×10^{-29} cm^2 molecule sr^{-1}) can be attained in a trapped droplet 4 μm in radius if the system is fully optimised for sensing species by spontaneous Raman.[21] This detection limit is determined by bit-noise in the analogue-to-digital signal conversion step. An order of magnitude improvement is achievable if the signal were to be amplified prior to a digitisation step, a detection limit equivalent to ~10 mM nitrate in aqueous solution.

In this publication, we will explore the sensitivity of an AOT instrument to sample free-flowing aerosol particles by coalescence sampling. In Section II we review the experimental implementation of AOT including the spectroscopic analysis, the typical accuracies of measurements, and the sensitivities this provides for sampling free-flowing aerosol by coalescence sampling. A simple framework for estimating the flux at which aerosol mass is accreted by a sampling droplet from a flowing aerosol is discussed in Section III. In Section IV we present measurements that explore the stability and sensitivity for coalescence sampling.

Experimental Description and Sensitivities

A commercial aerosol optical tweezers (Biral, AOT-100) is used in this work.[39] A single optical trap is formed from a tightly focussed laser beam at 532 nm.[8,16] The instrument is equipped with a 500 mm focal length spectrograph (using a 1200 $g\cdot mm^{-1}$ diffraction grating) and charge coupled device detector for recording Raman scattering from the trapped droplet. All spectra are acquired with a 1 s integration time. The relative

humidity (RH) in the trapping cell is controlled by mixing flows of humidified and dry nitrogen and is measured on the outflow from the cell with an accuracy of ±2 % (Honeywell HIH-4602C). The optical trap is first loaded with a sodium chloride droplet of ~5 μm radius, referred to as the sampling droplet, from aerosol generated by an ultrasonic nebuliser; aqueous sodium chloride droplets are mostly used as sampling droplets although any aqueous-solute system could be used. For the coalescence sampling studies, the aerosol flow is generated either with an ultrasonic nebuliser to generate coarse mode aerosol or from a constant output atomiser (TSI, Model 3076) to generate particles <1 μm in diameter.

The Raman spectra are analysed as the measurement proceeds to allow real-time monitoring of the sampling droplet size and n-RI from the stimulated Raman intensity, as well as composition through spontaneous Raman intensity measurements. The analysis algorithms for determining size and n-RI have been discussed extensively before, along with expected levels of uncertainties.[18,19] Figure 1 shows a typical measurement of the stability in the size, n-RI and composition (spontaneous Raman band intensity of the O-H stretching band of water) of a sample droplet over a period of 200 s. Typical reproducibilities are shown in Figure S1 for retrieved size, n-RI and composition (as a fraction of a peak ratio) acquired at 1 s intervals over a 200 s period with standard deviations of ±1.0 nm, 0.0003 and 0.01, respectively. It should be noted that there is no size dependence to these uncertainties over the range considered (an 1800 nm change in sample droplet size). Measurements over a longer integration time (e.g. 10 s rather than 1 s) can lead to improvements in these already low-noise determinations.

At this point, it is appropriate to consider the sensitivity of the AOT technique for coalescence sampling based on these typical stabilities and accuracies in radius, n-RI and spontaneous Raman measurements of composition. The flow of free aerosol will lead to a gradual accretion of species mass in the sampling droplet over time. We first consider the sensitivity of the measured size to the accreting flux. In Figure S2(a) and (b) we report the number of particles of varying size that must coalesce with the sampling droplet, either of radius 3 or 8 μm, to achieve a change in size of 2, 3 or 5 nm. Although these very small tolerances in droplet size change may be perceivable only just within the measurement accuracy of the technique, it should be noted here that we will be looking for a coincidence signature arising from simultaneous/correlated changes in radius,

n-RI and composition in any analysis. For each radius change, the corresponding increase in droplet volume was calculated and converted into a mass increase, assuming that the small amount of accreted material incorporated in to the sampling droplet leads to negligible change in the droplet density. The accreting aerosol mass is assumed to be intercepted by the sampling droplet in a dry state and have no associated hygroscopicity; any additional absorption of water by the accreting aerosol would lead to larger size changes. Typically between 1 and a few thousand particles are required for the detection threshold to be surpassed.

To examine the sensitivity to change in n-RI, we calculate the number of accreting aerosol particles of different n-RI to the sampling droplet that must be sampled to lead to changes in n-RI of 0.0005, 0.0007 and 0.0009. Using a volume weighted refractive index mixing rule (see Section SI.1), the volume fraction of the aerosol required to increase the sample droplet n-RI by each of these amounts was determined. Although a volume weighting mixing rule neglects to include the non-ideality of mixing (with associated influences on water uptake and non-additivity in mixture density), we are concerned here with only an estimation of measurement sensitivities.[40] Once again, we assume that the density of the droplet is unaffected by incorporation of the small amount of accreted aerosol needed to raise the refractive index; then, the increase in droplet volume can be converted into a number of coalescing aerosol particles that give rise to the increase in n-RI, Figures S2(c) and (d). The n-RI of aqueous NaCl is taken at a wavelength of 650 nm, in line with the n-RI retrieved from the cavity enhance Raman spectrum (CERS) fitting of WGM peaks on the Raman OH band. For the accreted aerosol, we assume a refractive index of 1.425, a typical value for organic aerosol.[40]

As expected, a larger number of accreted particles are required when the sampling droplet is larger to achieve both resolvable changes in size and n-RI. If 100 nm diameter aerosol particles are sampled, 400 – 2000 particles are required for a detectable change in size and n-RI, depending on the threshold sensitivities for a 3 μm radius sampling droplet, corresponding to an accreted mass of 0.2 – 1.0 pg. For an 8 μm radius sampling droplet, 3000 – 30000 particles are required, yielding an accreted mass of 1.5 to 15 pg. Assuming a solution density of 1 g cm^{-3}, the initial sampling droplets of 3 and 8 μm have masses of ~110 and 2140 pg, respectively.

Estimations of Expected Accretion Flux for Sampling Droplet

We present an overview of estimates of the expected accretion flux here; for details, the reader is referred to Section SI.2. Briefly, to estimate an accretion flux, we assume that the flowing aerosol size distribution can be described by a log-normal distribution in particle diameter. Typical representative size distributions used in this work are shown in Figure 2(a). From the flow rate of gas carrying the ambient aerosol, the mass flux of aerosol into the optical tweezers cell (schematic shown in inset to Figure 2(b)) can be calculated. At the centre of the cell, in the vicinity of the sampling droplet, the cell cross-section can be approximated as the product of the height and diameter. The cross-sectional area of the droplet is dependent on the droplet radius. Then, the fractional area of the aerosol flow intercepted by the sampling droplet can be estimated, yielding the accreted mass of aerosol sampled by the trapped droplet per second. For the cell used here, the fraction of aerosol intercepted is estimated to be as low as 5×10^{-7} (5×10^{-5} %). Judicious choice of cell design and aerosol delivery would increase the capture efficiency and accretion flux; our objective here is to provide a proof of concept study. Finally, the change in solute mass within the sampling particle over a specified time interval can be determined.

Estimates of the accretion rate with varying aerosol number concentration are shown in Figure 2(b) for distributions with mean diameters of 125 and 225 nm and number concentrations between 2×10^{3} and 2×10^{6} cm^{-3}, typical of the experimental values reported later. These distributions span a mass concentration range from 10 μg m^{-3} to 65 mg m^{-3}. A density for the accumulation mode aerosol of 1 g cm^{-3} is assumed. An aqueous sodium chloride sampling droplet is considered, 4.5 μm in radius at 80 % RH (corresponding to a *MFS* of 0.23 and a dry particle of 88 pg of NaCl, i.e. 380 pg of solute and water). For these aerosol size distributions and number concentrations, the mass flux accreted by the sampling droplet is in the range of 1×10^{-5} to 0.1 pg s^{-1}. Over a 10 minute period and with an aerosol concentration of 100,000 cm^{-3}, the solute mass accreted from the aerosol flow increases to a fraction of the total droplet solute mass of ~0.003 for the 125 nm distribution and ~0.02 for the 225 nm distribution. These fractions are equivalent to 0.29 to 1.7 pg of accreted aerosol mass for the two size distributions, or 0.5 and 3 fg s^{-1}. These fractions and accreted masses are detectable based on the sensitivities for measurements of size, n-RI and Raman intensity composition discussed in Section II.

The two accretion rates for the two size distributions considered above are for aerosol mass concentrations of 4.9 and 28 mg m^{-3} (for the 125 and 225 nm mean diameter distributions, respectively), a factor of ~1000 higher than typical ambient levels of aerosol. However, we have made no effort here to optimise the design of the aerosol cell for collection efficiency, currently only 5×10^{-7} (5×10^{-5} %). Improved sensitivity could be achieved through improved cell design, reducing the cross-section of the aerosol flow at the trap site. In addition, methods for concentrating aerosol flows using virtual impactors could be combined with the AOT sampling approach.

Results and Discussion

The accretion of aerosol mass by the sampling droplet leads to a change in the relationship between particle size and n-RI. As a first step towards using an optically trapped droplet as a sample volume, we discuss the stability in the sampling droplet size and n-RI and the reproducibility with variation in RH. We then consider signatures of coalescence sampling when the flowing aerosol has a mass median diameter in the coarse mode, generated by an ultrasonic nebuliser, demonstrating that the sampling can discriminate between particles of like and dissimilar composition. Finally, we report preliminary measurements of sampling for accumulation mode aerosol generated by an atomiser.

Stability and Reproducibility in Sample Droplet Size and n-RI

The initial loading of the optical trap with an aqueous sodium chloride droplet leads to sampling droplets of dry particle size (dry solute masses) that vary from measurement-to-measurement. However, all sampling droplets will have a well-defined n-RI at a particular RH, a consequence of the well-defined relationship between n-RI and solute concentration (here, Na^+ and Cl^- concentrations) or water activity and the independence of surface curvature for droplets in the coarse mode size range. This leads to a well-defined trajectory in the dependence of n-RI on the wet droplet radius, r_{wet}, for all measurements made on the same droplet.[28,29] For convenient comparison of measurements made with different sampling droplets, the time-dependence in radius (during which there may be fluctuations in RH) must be represented on a common normalised scale to factor out the variation in dry particle radius, r_{dry}. To achieve this, the diameter growth factor, $GF_d(RH)$ is determined,[16] as described in Section SI.3, where $GF_d(RH)$ is given by:

$$GF_d(RH) = \frac{r_{wet}}{r_{dry}} \qquad (1)$$

A typical measurement of the evolving radius, n-RI, density and *MFS* for a sodium chloride sample droplet is shown in Figure S4 with RH varied in the range 72 to 96 %, driving water evaporation and condensation and change in growth factor. Rather than normalising all data to a reference time period, point by point fluctuations in the n-RI retrieved from the Raman fitting are used explicitly to illustrate the level of uncertainty observed in inferring the droplet density, mass fraction of solute and dry size. Although the wet size varies by ~1500 nm as the RH changes, the standard deviation on the estimated dry size is only 12 nm.

In Figure 3 we present typical measurements (3 different droplets) of the variation in n-RI with diameter growth factor for aqueous sodium chloride sampling droplets over a wide range in RH from ~95.7% (n-RI of 1.345 and GF_d of 2.90) to 49 % (n-RI of 1.410 and GF_d of 1.420). The n-RI data are represented by a fourth-order polynomial in GF_d, and the residuals from the fit are shown. These data clearly illustrate the level of reproducibility that can be achieved from measurement-to-measurement in the determination of the relationship between droplet radius (GF_d) and n-RI. The standard deviation in the residual in n-RI is $\pm 5\times10^{-4}$ (±0.036 %), well within the expected uncertainty estimated from our previous simulations.[19] In this previous work, we estimated that random Gaussian noise in the wavelength of the WGMs with a standard deviation of 0.02 nm (a typical level of uncertainty for the particular spectrograph and diffraction grating used here) would lead to an uncertainty in the retrieved value of n-RI of $\pm 6.5\times10^{-4}$. Similarly, our expectation from this earlier work was an uncertainty in size of ±2.2 nm or ±0.055 % for a droplet of size 4 μm. For a particle of typical dry size ~2 μm, this corresponds to an uncertainty in GF_d of ~±0.001. Although the errors in the size and n-RI are comparable in percentage terms, GF_d can typically vary by 1 unit or more whereas the value of n-RI varies by little more than 0.1. Thus, in examining the reproducibility of the growth curve/n-RI relationship, the uncertainty in the retrieved n-RI value always limits the overall resolution and sensitivity of the measurement.

Coalescence Sampling of Coarse Mode Aerosol

Figure 4 presents an example of a coalescence sampling experiment with an aqueous sodium chloride droplet as the sampling droplet with a nebulised flow of aqueous sodium chloride aerosol introduced at ~2000 s. The time-dependence of the droplet size and n-RI are shown; uncertainties in size and n-RI are consistent with the

previous stability studies. The wet radius of the sample droplet increased significantly (by ~200 nm) over a narrow time window of <200 s. Remarkably, the value of the n-RI stayed constant even though solute mass had been introduced, reflecting that the RH of the gas phase was maintained at a constant level and ensuring that the actual water/NaCl balance in the droplet (i.e. the *MFS* or concentration) remained the same. Small variations in RH (e.g. around 3000 s) led to commensurate changes in n-RI. By contrast, the dry size of the particle increased from ~2880 to ~2980 nm, reflecting the additional sodium chloride mass accreted by through coalescence. This accretion of mass is equivalent to the addition of a single solute particle of ~1370 nm radius.

After ~4000 s, the sample droplet was exposed to a nebulised flow of aqueous sucrose droplets. On this occasion, not only did the size of the wet droplet increase, but n-RI increased markedly, reflecting the addition of a high n-RI component (n-RI = 1.558, pure component value) with less associated water than with sodium chloride at the RH of this experiment. After this time, the dry size (calculated from the procedure outlined above) should only be taken as indicative: this would only be equivalent to the true dry size if the accreted solute were of equal n-RI and hygroscopicity to the aqueous sodium chloride sampling droplet. The Raman spectrum clearly indicates that a distinct sucrose component has been added with a clear increase in the intensity of Raman scatter in the C-H region of the Stokes scattering.

In addition to the clear identification of coalescence sampling that can be achieved from such single point measurements, the overall variation in the n-RI/GF_d relationship with RH provides further information on the sampled mass. As an example, we consider the sequence of measurements shown in Figure 5. Prior to coalescence sampling of aerosol, a hygroscopic growth curve for the trapped sodium chloride droplet was recorded with change in RH from ~90 to ~60 %, with measurements of radius, n-RI and Raman intensities and with retrievals of dry size. Then, after ~18000 s, the sampling droplet was exposed to a flow of sucrose aerosol and coalescence observed, leading to change in size, n-RI and Raman intensity, and a clear change in the apparent dry size. After coalescence sampling, the hygroscopic growth of the sampling droplet was reanalysed by exposing the droplet to a time-dependent variation in RH.

An expanded view of the coalescence sampling period around 17500 s is shown in Figure S5. Notably a change in the Raman intensity ratio of 2 % is observed with considerable potential to monitor much smaller changes

when the intensity ratio is calculated with a rolling average over 100 s. The change in droplet size from 5435 nm to 5465 nm after coalescence sampling corresponds to the addition of solution aerosol with a total size of ~1390 nm. The diameter growth factor of sucrose solution is ~ 1.2 at 82% at sampling RH, corresponding to the addition of an amount of sucrose solute equivalent to a dry particle of ~1160 nm or 10.3 pg assuming volume additivity (with the density of sucrose assumed to be 1.581 g cm^{-3}). From the initial dry size of the sampling droplet, the mass of sodium chloride solute in the droplet is ~221 pg prior to sampling of the sucrose aerosol.

The time-evolving relationship between n-RI and GF_d inferred over the whole experiment is included in Figure 3 as recorded from the measurements of hygroscopic growth cycles both prior to and post the coalescence sampling period. A clear separation of the growth relationships in n-RI is apparent, providing a further opportunity to refine the detection and analysis of aerosol sampled by coalescence. It should be noted that the growth factor is calculated based on an average of the dry size of the sodium chloride solute in the particle alone; no correction is made for the addition of sucrose solute mass. This approach is chosen to represent the data as it clearly allows the identification of sampling events and a change in composition of the sampling droplet.

Coalescence Sampling of Accumulation Mode Aerosol

Having established the clear signature of coalescence sampling that can be determined from accreting coarse mode aerosol; we now provide a first demonstration of the application of this approach in sampling accumulation mode aerosol. A schematic of the experiment is shown in Figure S6. Sucrose aerosol was generated with the atomiser and dried with a Nafion drying tube (Perma Pure PD-100T-12SS), which reduced the RH of the aerosol flow to <5 %. This ensured that as much water as possible was removed from the initially wet aerosol, facilitating greater control and stability in the eventual RH at which the aerosol was introduced to the optical tweezers by isolating it from any drifts in water activity that arise at atomisation. Once dried, the aerosol was re-humidified with 4 saturators in sequence; each saturator consisted of a 15 cm long horizontally-orientated cylindrical cell (diameter 3 cm) half-filled with water. In each saturator, the aerosol flow passed over the water surface leading to an RH >90 %. The aerosol flow was then mixed with dry nitrogen to set the RH at which the aerosol was introduced to the optical tweezers. On the outflow from the optical tweezers,

measurements of aerosol size distribution were made with a differential mobility analyser (DMA; GRIMM Aerosol Technik, Vienna/Reischl type, L-DMA) and a condensation particle counter (CPC; GRIMM Aerosol Technik, Model 5.403), Figure 6(a), with the mass concentration of the aerosol in this example equal to 104.6 mg m^{-3}. A simulated log-normal size distribution is also shown in Figure 6(a) with a mean particle diameter of 220 nm, a standard deviation of 1.65, a number concentration of 6.9×10^6 cm^{-3} and a marginally higher mass concentration (119 mg m^{-3}) than measured. In Figure 6(b), we report the time-dependence in the Raman intensity ratio and offset in n-RI for the tweezed droplet during the sampling period (equivalent to δn in equation (S2)). The offset in n-RI is derived from the difference between the measured n-RI at any instant in time and the expected n-RI based on the known variation in n-RI with droplet size from the dependence shown in Figure 3. The Raman intensity ratio and the offset in n-RI show the same qualitative trend with time as sucrose aerosol is accreted from the atomised flow.

From the n-RI change and the Raman intensity change, we can estimate the accreted mass of sucrose aerosol using the approach described in Section II and equation (S3). The n-RIs of aqueous sodium chloride aerosol and aqueous sucrose aerosol at 80 % RH, the RH of the experiment, are 1.3717 and 1.465, respectively, with mass fractions of solute of 0.23 and 0.72 and densities of 1.17 and 1.33 g cm^{-3} for these two aerosol droplet solutions. Thus, the volume fraction of accreted aerosol in the sampling droplet can be inferred from the n-RI change of 0.0173 as 0.185. For the initial sodium chloride sampling droplet, 4.5 μm radius, this corresponds to an accreted volume of aqueous-sucrose aerosol of 7.1×10^{-17} m^3, or a new droplet radius of 4.762 μm. The accreted mass of aqueous-sucrose aerosol is 94.4 pg, or 68.0 pg of sucrose. The initial mass of the sampling droplet is 447 pg with a mass of water of 343 pg, making a total of 369 pg of water in the final droplet. In summary, 68 pg of sucrose is accreted in 1000 s from an aerosol with a mass loading of 104.6 mg m^{-3}. This is equivalent to 0.068 pg s^{-1} or 6.5×10^{-4} pg s^{-1} / mg of aerosol mass concentration from a size distribution which peaks at a diameter of ~220 nm and with a number concentration of 6.9×10^6 cm^{-3}. The accretion flux can be estimated from equation (S8) for the simulated size distribution shown in Figure 6(a). With an aerosol flow rate through the cell of 200 cm^3 min^{-1} and at a RH of 80 % with a mass fraction of sodium chloride of 0.2 in the sampling droplet of initial radius 4.5 μm, the predicted accretion flux is 0.126 pg s^{-1}. This compares extremely well (within a factor of 2) to that measured of 0.068 pg s^{-1}.

Conclusions

We have examined the potential of using an optically tweezed aerosol droplet as a sampling volume for accreting, detecting and quantifying free-flowing aerosol of accumulation and coarse mode size. Real-time measurements of the stability in size, n-RI and composition of a sampling droplet prior to introduction of the aerosol flow confirm that these quantities can be measured with high accuracy and low noise. Typical standard deviations in size and n-RI, retrieved from the Raman fingerprint of WGMs over a period of 200 s, are $<\pm 2$ nm and $<\pm 0.0005$, respectively, equivalent to $<\pm 0.04$ % in both measured quantities. Similarly, the measured spontaneous Raman intensity of an O-H or C-H band has a standard deviation of $<\pm 1$ % over a 200 s period and this could be significantly improved by signal averaging over a time-integration window of longer than 1 s. Such high stability facilitates highly accurate measurements of accretion flux. In benchmark experiments with coarse mode aerosol, discrete coalescence sampling events can be observed with clear signatures in changes in size, n-RI and Raman band intensities observed for accretion masses of 10 pg. To probe the lowest detection limit accessible, measurements of the steady accretion of mass from an accumulation mode aerosol flow have shown that fluxes as low as 0.068 pg s^{-1} can be detected over a 50 s period, equivalent to ~3 pg of sampled material (see Figure 6(b)). These detection thresholds are consistent with our expectations based on the sensitivity analysis provided in Section II. Currently, such an accreted mass can only be detected over a reasonable time frame by using high mass concentrations of aerosol. Future work will focus on improving the collection efficiency of the sampling droplet by targeted delivery of the aerosol flow and by using an aerosol concentrator.

Acknowledgements

JPR, REHM and AEH acknowledge support from DSTL through contract DSTL/AGR/00264/01. JPR and BRB acknowledge support from the EPSRC for funding grant EP/L010569/1. The experimental data are provided through the University of Bristol data repository at Reid, J.P. (2017): Optical Properties of Aerosol, University of Bristol, DOI: 10.5523/bris.1ttc1y9kic0311l7c5n2oq45oe.

Supporting Information. Further examples of coalescence sampling measurements, a summary of the uncertainty in measurements of size, n-RI and Raman intensities, and the equilibrium variations in n-RI, density and mass fraction of solute for sodium chloride aerosol are presented.

References

(1) McMurry, P. H. *Atmos. Environ.* **2000**, *34* (12-14), 1959–1999.

(2) Prather, K. A; Hatch, C. D.; Grassian, V. H. *Annu. Rev. Anal. Chem. (Palo Alto. Calif).* **2008**, *1*, 485–514.

(3) Hallquist, M.; Wenger, J. C.; Baltensperger, U.; Rudich, Y.; Simpson, D.; Claeys, M.; Dommen, J.; Donahue, N. M.; George, C.; Goldstein, A. H.; Hamilton, J. F.; Herrmann, H.; Hoffmann, T.; Iinuma, Y.; Jang, M.; Jenkin, M. E.; Jimenez, J. L.; Kiendler-Scharr, A.; Maenhaut, W.; McFiggans, G.; Mentel, T. F.; Monod, A.; Prevot, A. S. H.; Seinfeld, J. H.; Surratt, J. D.; Szmigielski, R.; Wildt, J. *Atmos. Chem. Phys.* **2009**, *9* (14), 5155–5236.

(4) Bzdek, B. R.; Pennington, M. R.; Johnston, M. V. *J. Aerosol Sci.* **2012**, *52*, 109–120.

(5) Sullivan, R. C.; Prather, K. A. *Anal. Chem.* **2005**, *77* (12), 3861–3885.

(6) Laskin, J.; Laskin, A.; Nizkorodov, S. A. *Int. Rev. Phys. Chem.* **2012**, *32* (1), 128–170.

(7) Flagan, R. C. *Aerosol Sci. Technol.* **1998**, *28* (4), 301–380.

(8) Miles, R. E. H. E. H.; Carruthers, A. E. E.; Reid, J. P. P. *Laser Photon. Rev.* **2011**, *5* (4), 534–552.

(9) Després, V. R.; Alex Huffman, J.; Burrows, S. M.; Hoose, C.; Safatov, A. S.; Buryak, G.; Fröhlich-Nowoisky, J.; Elbert, W.; Andreae, M. O.; Pöschl, U.; Jaenicke, R. *Tellus, Ser. B Chem. Phys. Meteorol.* **2012**, *64*, 15598.

(10) Haisch, C. *Meas. Sci. Technol. Meas. Sci. Technol* **2012**, *23*, 12001–12017.

(11) Moise, T.; Flores, J. M.; Rudich, Y. *Chem. Rev.* **2015**, *115*, 4440–4439.

(12) Nozière, B.; Kalberer, M.; Claeys, M.; Allan, J.; D'Anna, B.; Decesari, S.; Finessi, E.; Glasius, M.; Grgić, I.; Hamilton, J. F.; Hoffmann, T.; Iinuma, Y.; Jaoui, M.; Kahnt, A.; Kampf, C. J.; Kourtchev, I.; Maenhaut, W.; Marsden, N.; Saarikoski, S.; Schnelle-Kreis, J.; Surratt, J. D.; Szidat, S.; Szmigielski, R.; Wisthaler, A. *Chem. Rev.* **2015**, *115* (10), 3919–3983.

(13) Magnusson, L. E.; Risley, D. S.; Koropchak, J. A. *J. Chromatogr. A* **2015**, *1421*, 68–81.

(14) Parshintsev, J.; Hyötyläinen, T. *Anal. Bioanal. Chem.* **2015**, 5877–5897.

(15) Hamilton, J. F.; Lewis, A. C.; Carey, T. J.; Wenger, J. C. *Anal. Chem.* **2008**, *80* (2), 474–480.

(16) Krieger, U. K.; Marcolli, C.; Reid, J. P. *Chem. Soc. Rev.* **2012**, *41* (19), 6631–6662.

(17) Reid, J. P. J. P. *J. Quant. Spectrosc. Radiat. Transf.* **2009**, *110* (14-16), 1293–1306.

(18) Preston, T. C.; Reid, J. P. *J. Opt. Soc. Am. A* **2015**, *32* (11), 2210.

(19) Preston, T. C.; Reid, J. P. *J. Opt. Soc. Am. B* **2013**, *30* (8), 2113–2122.

(20) Miles, R. E. H.; Walker, J. S.; Burnham, D. R.; Reid, J. P. *Phys. Chem. Chem. Phys.* **2012**, *14* (9), 3037–3047.

(21) Meresman, H.; Hudson, A. J.; Reid, J. P. *Analyst* **2011**, *136* (17), 3487–3495.

(22) Dennis-Smither, B. J.; Miles, R. E. H.; Reid, J. P. *J. Geophys. Res.* **2012**, *117* (D20), D20204.

(23) Reid, J. P.; Dennis-Smither, B. J.; Kwamena, N.-O. A.; Miles, R. E. H.; Hanford, K. L.; Homer, C. J. *Phys. Chem. Chem. Phys.* **2011**, *13* (34), 15559–15572.

(24) Kwamena, N.-O. a. N.-O. A.; Buajarern, J.; Reid, J. P. *J. Phys. Chem. A* **2010**, *114* (18), 5787–5795.

(25) Stewart, D.; Cai, C.; Nayler, J.; Preston, T. C.; Reid, J. P.; Krieger, U.; Marcolli, C.; Zhang, Y.-H. *J. Phys. Chem. A* **2015**, *119*, 4177–4190.

(26) Hargreaves, G.; Kwamena, N.-O. A. O. A.; Zhang, Y. H.; Butler, J. R.; Rushworth, S.; Clegg, S. L.;

Reid, J. P. *J. Phys. Chem. A* **2010**, *114* (4), 1806–1815.

(27) Lienhard, D. M.; Bones, D. L.; Zuend, A.; Krieger, U. K.; Reid, J. P.; Peter, T. *J. Phys. Chem. A* **2012**, *116* (40), 9954–9968.

(28) Cai, C.; Stewart, D. J.; Preston, T. C.; Walker, J. S.; Zhang, Y.-H.; Reid, J. P. *Phys. Chem. Chem. Phys.* **2014**, *16* (7), 3162–3172.

(29) Cai, C.; Stewart, D. J.; Reid, J. P.; Zhang, Y.; Ohm, P.; Dutcher, C. S.; Clegg, S. L. *J. Phys. Chem. A* **2015**, *119*, 704–718.

(30) Bzdek, B. R.; Power, R. M.; Simpson, S. H.; Reid, J. P.; Royall, C. P. *Chem. Sci.* **2016**, *7*, 274–285.

(31) Power, R. M.; Simpson, S. H.; Reid, J. P.; Hudson, A. J. *Chem. Sci.* **2013**, *4* (6), 2597–2604.

(32) Power, R. M.; Reid, J. P. *Reports Prog. Phys.* **2014**, *77* (7), 074601.

(33) Wills, J. B.; Knox, K. J.; Reid, J. P. *Chem. Phys. Lett.* **2009**, *481* (4-6), 153–165.

(34) Reid, J. P.; Meresman, H.; Mitchem, L.; Symes, R. *Int. Rev. Phys. Chem.* **2007**, *26* (1), 139–192.

(35) Reid, J. P.; Mitchem, L. *Annu. Rev. Phys. Chem.* **2006**, *57*, 245–271.

(36) Butler, J. R.; Wills, J. B.; Mitchem, L.; Burnham, D. R.; McGloin, D.; Reid, J. P. *Lab Chip* **2009**, *9* (4), 521–528.

(37) Mitchem, L.; Buajarern, J.; Ward, A. D.; Reid, J. P. *J. Phys. Chem. B* **2006**, *110* (28), 13700–13703.

(38) Dennis-Smither, B. J.; Marshall, F. H.; Miles, R. E. H.; Preston, T. C.; Reid, J. P. *J. Phys. Chem. A* **2014**, *118* (30), 5680–5691.

(39) Davies, J. F.; Wilson, K. R. *Anal. Chem.* **2016**, *88*, 2361–2366.

(40) Cai, C.; Miles, R. E. H.; Cotterell, M. .; Marsh, A.; Rovelli, G.; Rickards, A. M. J.; Zhang, Y. H.; Reid, J. P. *J. Phys. Chem. A* **2016**, *120*, 6604−6617.

(41) Seinfeld, J. H.; Pandis, S. N. *Atmospheric Chemistry and Physics: From Air Pollution to Climate Change*; Wiley & Sons: New York, 2006.

Figures

Figure 1: Measurements of size, n-RI and Raman intensities over 200 s for an aqueous sodium chloride sampling droplet.

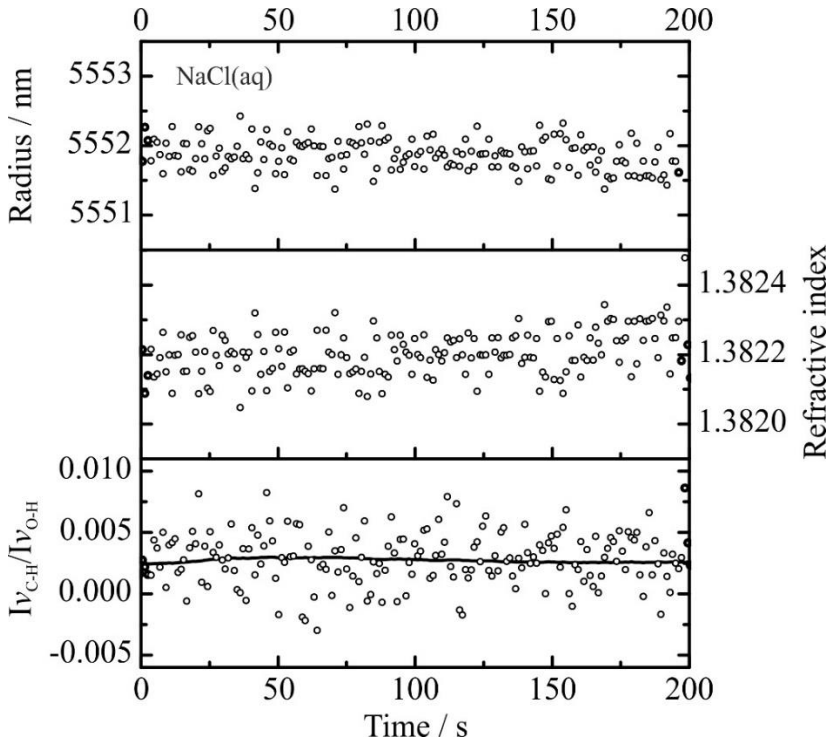

Figure 2: (a) Simulated size distributions for accretion flux estimates for size distributions with mean diameters of 125 (black) and 225 nm (red), and with number concentrations of 2.2×10^5 (dashed lines) and 2.2×10^6 cm^{-3} (solid lines). The standard deviations for the four distributions are 1.8. The inset shows schematically the dimensions of the AOT trapping cell. (b) Predicted fluxes of mass accreted by sampling droplet for different size distributions (red solid line, mean particle size 225 nm; black dotted line, mean particle size 125 nm) and fractional change in solute mass over a 10 minute sampling interval.

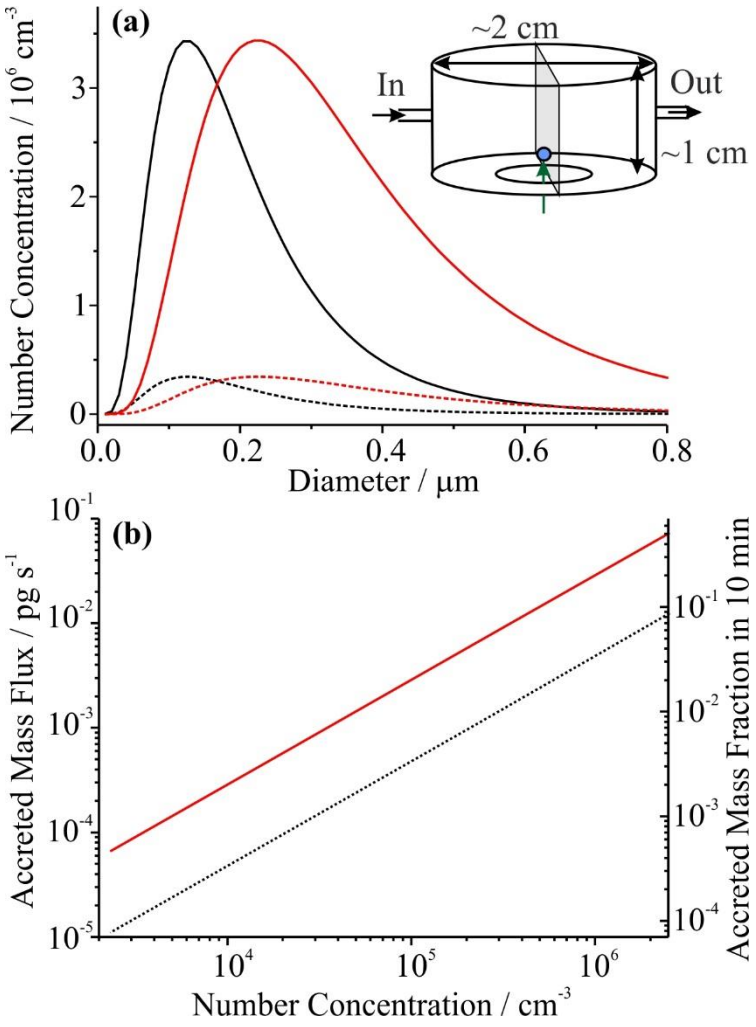

Figure 3: Comparison of the n-RI/growth factor relationships for the sampling sodium chloride droplet. Each symbol (blue squares, black circles, red triangles) represents a different experiment. A fit to all of the data for aqueous sodium chloride droplets is shown by the yellow line, with the residuals for each data set shown in the lower panel. The filled dark-blue squares (displaced from the yellow line) are measurements made following a period of coalescence sampling of sucrose aerosol, illustrating the resulting departure from the relationship between growth factor and refractive index measured for the sampling droplet.

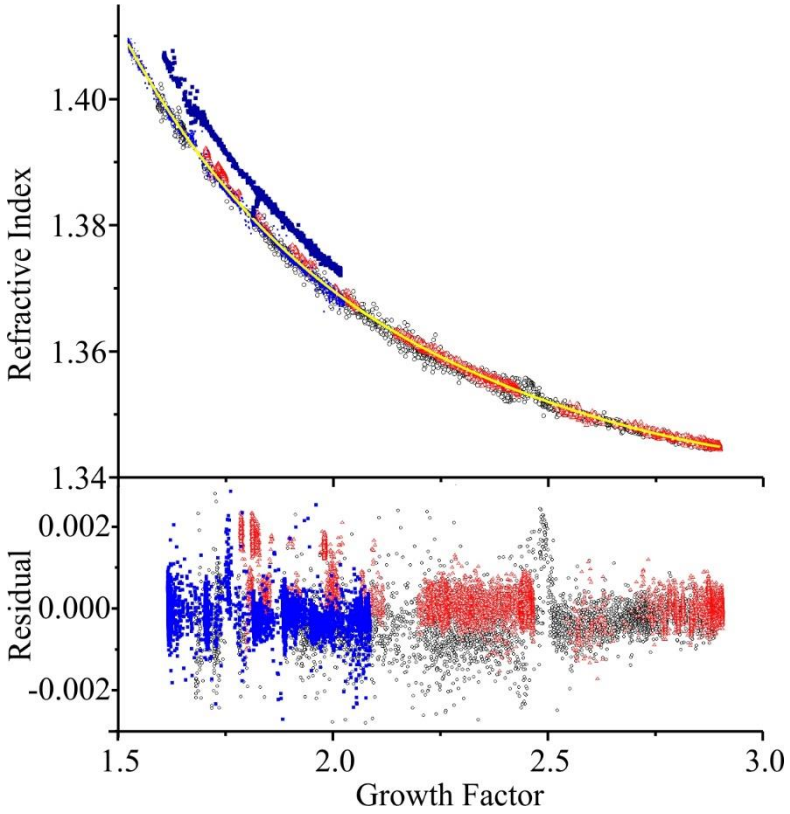

Figure 4: Example measurement of coalescence sampling. In the first coalescence window (first yellow box), a flow of aqueous sodium chloride droplets were introduced. In the second window, a flow of aqueous sucrose droplets were introduced.

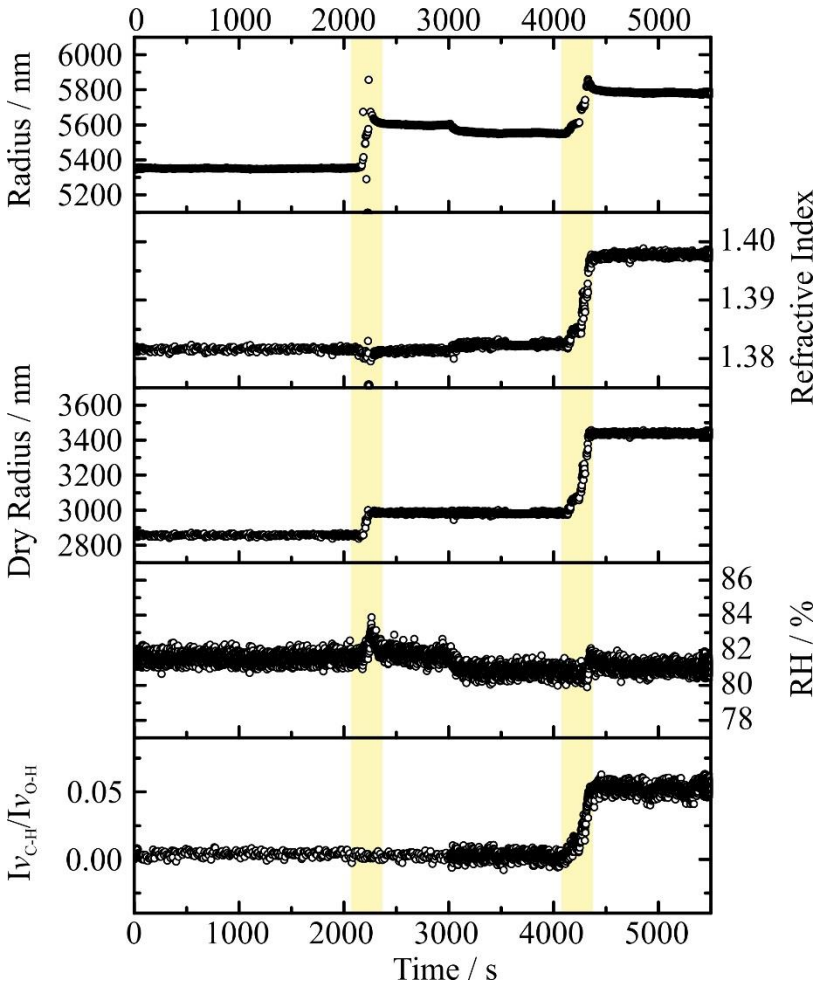

Figure 5: Example of a combined hygroscopic growth measurement of the sampling droplet (0 to ~15000 s) and coalescence sampling of aqueous sucrose aerosol (shown by yellow box) with a hygroscopic growth measurement following the coalescence event.

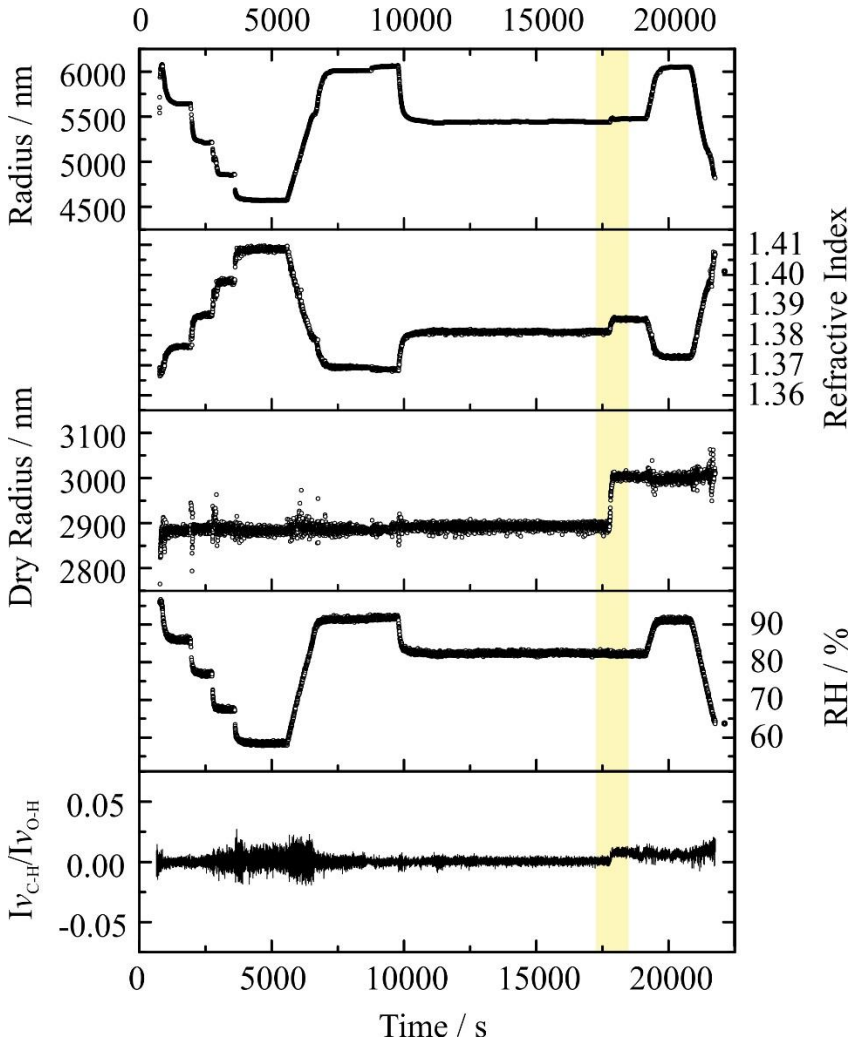

Figure 6: (a) The size distribution as measured by the DMA/CPC (black solid line) compared with a log-normal simulated distribution used in the analysis of instrument sensitivity (blue dashed line). (b) Time-dependence in offset in n-RI and Raman band intensities during sampling measurement.

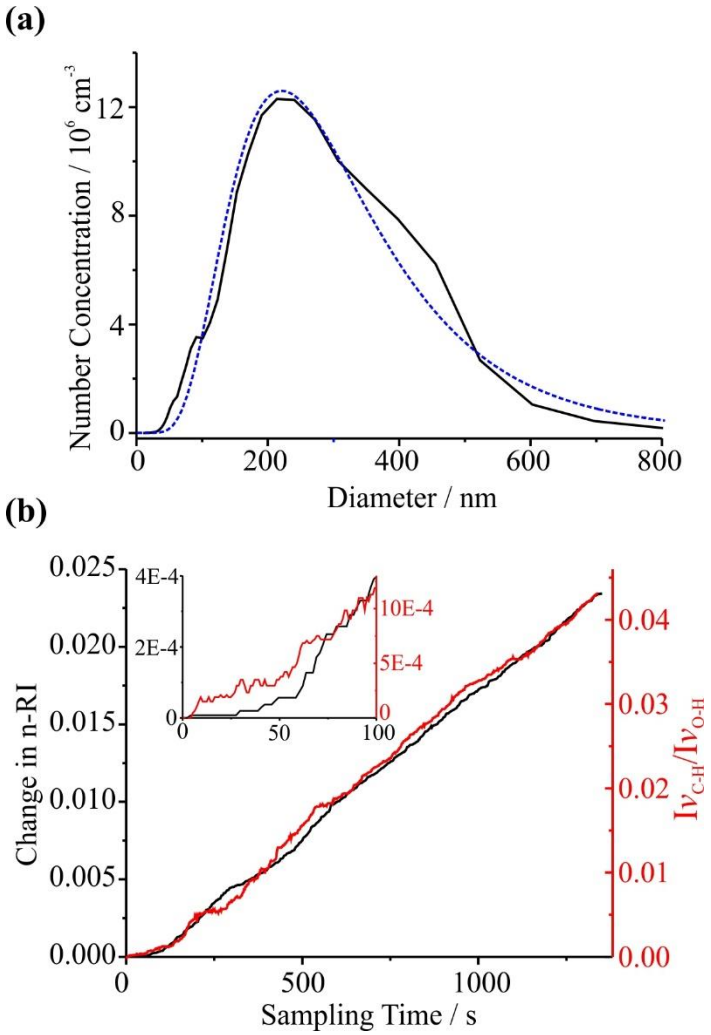

Table of Contents Graphic